

Electromechanical Brake Modeling and Control: From PI to MPC

Chris Line, *Member, IEEE*, Chris Manzie, *Member, IEEE*, and Malcolm C. Good, *Member, IEEE*

Abstract—The electromechanical brake (EMB) force control problem has been approached in prior work using cascaded proportional-integral (PI) control with embedded feedback loops to regulate clamp force, motor velocity, and motor current/torque. However, this is shown to provide limited performance for an EMB when faced with the challenges of actuator saturation, load-dependent friction, and nonlinear stiffness. There is a significant margin for improvement, and a modified control architecture is proposed using techniques of gain scheduling, friction compensation, and feedback linearization. A further improvement is then achieved by incorporating a model predictive control that better utilizes the available motor torque. Simulation and experimental results are presented to demonstrate the improvement in performance.

Index Terms—Cascaded proportional-integral (PI) control, electromechanical brake (EMB) model, electromechanical brakes (EMBs), feedback linearization, friction compensation, gain scheduling, model predictive control (MPC).

I. INTRODUCTION

THE potential for electromechanical brakes (EMBs) to succeed hydraulic brake systems has continued to attract the interest of automotive manufacturers and the brake research community. Part of the appeal is that EMBs offer the potential benefits of component reduction, system weight reduction, “plug, bolt, and play” modularity, improved brake performance, and a brake system that supports a drive-by-wire platform. There is potential for a more coordinated vehicle dynamics control with integrated “by-wire” operation of throttle, steering, and brakes. Two applications foreseeable in the immediate term are improved electronic stability programs and the provision of a system that is well suited to coordinate regenerative braking. Looking further ahead, the drive-by-wire concept provides a platform that may ultimately support autonomous vehicles.

Electromechanical disk brakes, such as the patent design shown in Fig. 1, typically comprise an electric motor driving a mechanism with rotary-to-rectilinear reduction to clamp and release the brake rotor. A wealth of information on the mechanical design of these actuators may be found in scores of patents that have originated from most of the major automotive

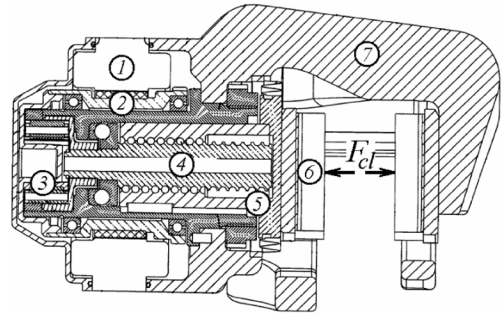


Fig. 1. WO 2005/124180 A1: actuating mechanism and brake assembly patented by PBR Australia Pty. Ltd. [1].

manufacturers. A number of these innovative prototypes have been deployed as foundation brakes on concept vehicles. While a consensus has yet to be established regarding the technology, some forecasts predict commercial introduction within coming decades. Already, related electromechanical park brakes have proven to be a successful forerunner for the commercialization of such technology.

In Fig. 1, a motor torque may be developed between the stator ① and the rotor ②. The motor rotor drives the planetary gear ③ and ball screw ④ to operate the piston ⑤ and clamp the brake pads ⑥. The brake clamp force F_{cl} is reacted over the bridge of the floating calliper ⑦ to the opposing brake pad.

EMB actuators are installed with a mechanical, power, and communications interface to the vehicle. Brake commands from the driver or vehicle dynamics controller are transmitted via an in-vehicle network that is based on a safety-critical, time-triggered communication protocol. Depending on how functionality is arranged between the central vehicle controller and the actuator control, brake instructions may command brake torque, brake force, or a particular mode of operation such as standby, off, or anti-lock braking. It is here that the EMB control problem is encountered; a control algorithm is required to respond to the brake commands and operate the brake actuator.

The EMB control problem is characterized by the challenges of a large operational range up to 40 kN, actuator saturation, load-dependent friction, and nonlinear stiffness. Some prior work on EMB control has followed the approach of a cascaded proportional-integral (PI) control architecture. An outer-loop force control and inner-loop motor current control is used in [2] and [3]. Meanwhile, cascaded clamp force, velocity, and current/torque control loops are described in [4]–[11].

This paper extends the earlier work, beginning with an investigation on how to optimally tune the control gains. It is found that a single set of fixed gains cannot cover the entire operational envelope satisfactorily. Further, degraded performance

Manuscript received June 9, 2006; revised March 9, 2007. Manuscript received in final form June 17, 2007. Recommended by Associate Editor I. Haskara. This work was supported by the Research Centre for Advanced By-Wire Technologies (RABiT) and its industry partner, Pacifica Group Technologies Pty. Ltd.

The authors are with the Research Centre for Advanced By-Wire Technologies, Department of Mechanical and Manufacturing Engineering, The University of Melbourne, Melbourne, Vic. 3010, Australia (e-mail: cjl@unimelb.edu.au; manziec@unimelb.edu.au; mcgood@unimelb.edu.au).

Digital Object Identifier 10.1109/TCST.2007.908200

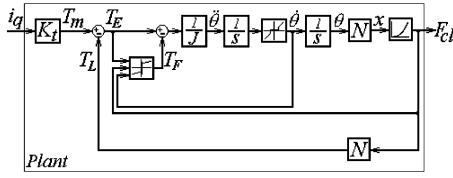


Fig. 2. EMB model relating input motor quadrature current to output clamp force.

is observed for fine maneuvers during brake operation due to the load-dependent friction. Consequently, a modified control architecture is proposed to address the plant nonlinearity with techniques of gain scheduling, friction compensation, and feedback linearization. A further improvement is then achieved with the inclusion of a model predictive controller that better utilizes the available motor torque. A simplification and relaxation of the constrained, nonlinear model predictive control (MPC) problem is followed to achieve a practical, real-time implementation on the embedded controller of a prototype EMB.

This paper is organized as follows. Section II presents the EMB model used for control design and simulation. Section III covers the problem of tuning the PI gains. Section IV contains proposed modifications to the control architecture. The inclusion of MPC is then considered in Section V. Simulation and experimental results are included to demonstrate the performance with the successive control modifications.

II. EMB MODEL

The simplified EMB model used for control design and analysis is shown in Fig. 2. The model input is the motor quadrature current i_q and the output is the brake clamp force F_{cl} . Related work on EMB modeling may be found in [4]–[9], [12], and [13].

The EMB model was used to describe a prototype actuator similar to that in Fig. 1. More generally, the model describes an electromechanical disk brake with a single motor drive and without brake “self-energization.” It is a “half” calliper model based on that in [9], and it assumes that the clamp force developed between one brake pad and the rotor is reacted over the bridge of the floating calliper by the opposing brake pad. The model considers a torque balance about the motor axis assuming lumped inertia, stiffness, and damping. The motor angular acceleration $\ddot{\theta}$ is determined by the effective moment of inertia J and torques due to the motor T_m , load T_L , and friction T_F as

$$T_m - T_L - T_F = J\ddot{\theta}$$

so that

$$i_q K_t - F_{cl} N - T_F = J\ddot{\theta} \quad (1)$$

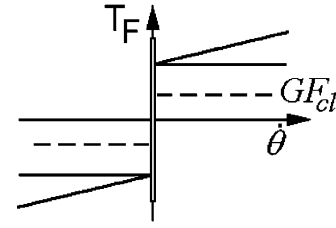


Fig. 3. Friction model is depicted as a friction-velocity map relating the friction torque T_F and the motor velocity $\dot{\theta}$. It has a load-dependent term GF_{cl} and describes viscous friction, Coulomb friction, and static friction at lockup.

where i_q is the motor quadrature current, K_t is the torque constant, F_{cl} is the brake clamp force, and N is the gear ratio.

The friction model is perhaps best described as a friction-velocity map with load dependency and lockup behavior. The friction torque T_F is modeled as a function of the motor angular velocity $\dot{\theta}$, brake clamp force F_{cl} , and the external torque T_E . The model is depicted in Fig. 3 and is given explicitly by (2), shown at the bottom of the page. Here, D is the viscous friction coefficient, C is the load-independent Coulomb friction torque, G is the friction load dependency, and T_s is the load-independent static friction torque. ε defines a small zero velocity bound in accordance with the Karnopp remedy for zero velocity detection [14]. This zero velocity bound for the friction model is depicted in Fig. 3. For consistency, the bound is also imposed on the velocity signal $\dot{\theta}$ in Fig. 2 following the integration of the motor angular acceleration $\ddot{\theta}$.

A nominal translation of the piston mechanism x is determined by the motor angular position θ and the reduction N . The clamp force F_{cl} is then given by a nonlinear stiffness.

The simplifying assumptions of the EMB model mean that it does not capture the secondary effects of friction presliding motion, internal mechanism compliance, nor viscoelastic stiffness. However, these effects are only marginally significant for describing the behaviour of macromotion brake maneuvers.

Prior to simulating the EMB, it was necessary to measure the model parameters. Bench-top tests were conducted with the prototype actuator operating on a clamp force measurement plate. The characteristic stiffness was determined from measurements of motor position and clamp force. While this is known to vary with pad wear and temperature [6], all experiments were run at room temperature and with the same unworn brake pads for consistency. With the zero position defined as the contact point between the brake pad and rotor, the measured stiffness from 0 to 40 kN was approximately described by

$$F_{cl} = \begin{cases} -7.23x^3 + 33.7x^2 - 3.97x, & x > 0.125 \\ 0.1295x, & \text{otherwise.} \end{cases} \quad (3)$$

Here, the clamp force F_{cl} is given in kilonewtons, and the nominal piston position x in millimeters.

$$T_F = \begin{cases} D\dot{\theta} + (C + GF_{cl})\text{sign}(\dot{\theta}), & \forall |\dot{\theta}| > \varepsilon \\ T_E, & \text{if } |\dot{\theta}| < \varepsilon \text{ and } |T_E| < (T_s + GF_{cl}) \\ (T_s + GF_{cl})\text{sign}(T_E), & \text{otherwise} \end{cases} \quad (2)$$

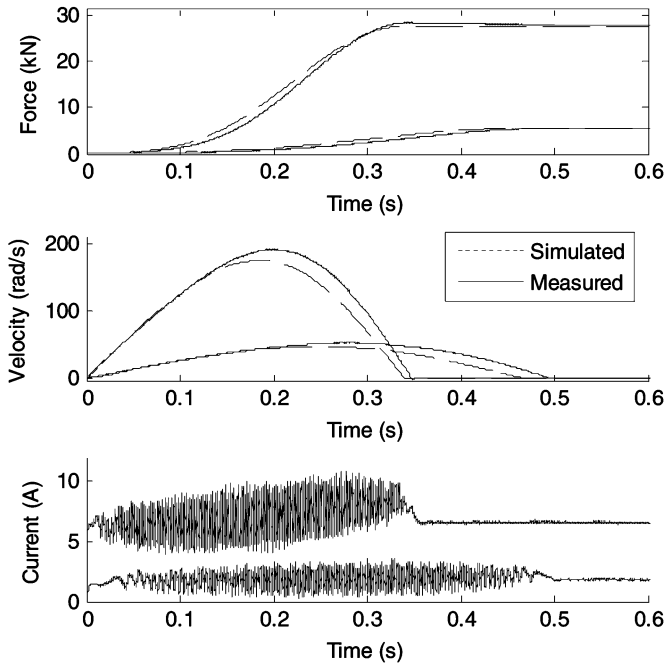


Fig. 4. Measured and simulated EMB responses to step motor current command.

The motor torque constant was determined at standstill from measurements of motor torque and the three-phase motor currents. Clark and Park transformations were applied to determine the motor quadrature current. For the experimental prototype used in this study, the torque constant was found to be $K_t = 0.0697 \text{ N}\cdot\text{m}/\text{A}$.

The load-independent static friction was measured in the clearance region from a series of breakaway tests as approximately $T_s = 0.0379 \text{ N}\cdot\text{m}$. The viscous friction coefficient was estimated from a series of constant velocity traverses across an extended clearance as $D = 3.95 \times 10^{-4} \text{ N}\cdot\text{m}\cdot\text{s}/\text{rad}$. The constant Coulomb friction offset was concurrently identified as $C = 0.0304 \text{ N}\cdot\text{m}$. The friction T_F was then determined over a series of applies using (1) and measurements of T_m , T_L , and $J\ddot{\theta}$. An estimate of the friction parameters could then be based on (2) for the state of motion $\forall|\dot{\theta}| > \varepsilon$. The friction load dependency was determined by a least-squares linear regression as $G = 1.17 \times 10^{-5} \text{ N}\cdot\text{m}/\text{N}$. This approach of linear regression can also render reasonable estimates for D and C .

The total gear ratio between the motor and the nominal piston position was calculated from the mechanism geometry as $N = 0.0263 \text{ mm}/\text{rad}$. Component masses were measured, and moments of inertia were calculated. Accounting for gearing, the effective system inertia seen by the motor was approximately $J = 0.291 \times 10^{-3} \text{ kg}\cdot\text{m}^2$.

Using the identified system parameters, the measured and simulated EMB responses are compared in Fig. 4. Two maneuvers are shown on the same plot for a low and higher quadrature-current input i_q . In each of the two maneuvers, the measured current was used as an input to the model. Results indicate a reasonable prediction of the states, both the motor velocity and

the brake clamp force. The model also predicts the transient and steady-state response with reasonable accuracy.

The model of the EMB mechanism may be extended with the addition of an electric motor circuit. While a three-phase motor circuit may be necessary for analysis of the electrical drive, as far as the mechanical dynamics are concerned, a single-phase equivalent motor model is sufficient to capture the effects of the back electromotive-force (EMF) and the limited supply voltage.

A single-phase equivalent motor circuit was used in this study, based on the model described in [9], with the back-EMF constant set as $2/3K_t$. The electrical circuit included a $0.05\text{-}\Omega$ resistance and a $56\text{-}\mu\text{H}$ inductance in series. There was a 42-V saturation on the maximum power supply voltage.

The simplified EMB model that is used in this paper for control design and simulation may also provide a useful tool for mechanical design. Part of its elegance is that the reduced set of model parameters is practical to identify for a particular electro-mechanical brake. Further, the model is found to predict brake maneuvers with reasonable fidelity.

III. BASELINE: CASCADED PI CONTROL FOR EMBS

To place the problem of EMB force control in context, a brief historical background is provided.

A. Historical Background

Early electromechanical motorcar brakes were driver-controlled using switches and variable resistors. One example from a patent in 1899 describes an electromagnetic drum brake with a “switch box” and a “suitable switch bar” to regulate the excitation current [15]. A second patent from the same year describes an electromagnetic disk brake with a switch to adjust a variable resistor and control the brake excitation [16]. Feedback position control was later introduced on some EMB designs. An early example is the motorized drum brake described in a 1914 patent with a control switch to adjust the commanded brake position [17].

While brake torque control would be preferred from the viewpoint of controlling vehicle dynamics, obtaining feedback measurements is challenging. For this reason, EMB rake designs have mainly deferred to brake clamp force control as the next best, or least removed, alternative.

Force control was pioneered in robotic mechanisms around the 1950s and 1960s [18]. One early application noted in Whitney’s 1985 “historical perspective” was the use of “electric-servo manipulators with force reflection” for remote radioactive hot lab work [18]. A “generic scheme” for force control was proposed by De Schutter in 1987 [19]. It generalized earlier approaches with an architecture that had outer-loop force control and cascaded inner control loops to successively manage position, velocity, and acceleration.

Around the same period a standard motion control architecture was established. Referencing works from the 1950s and 1960s, Leonhard states “there is general agreement that the most effective control scheme for drives is a cascaded or nested structure with a fast inner control loop” [20, p. 81]. A structure with

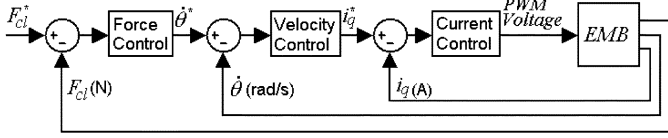


Fig. 5. EMB control architecture with cascaded force F_{cl} , velocity $\dot{\theta}$, and current i_q control loops.

control loops for position, velocity, and motor current was described. The inclusion of “feed-forward reference signals derived from an external reference generator” was also advocated for improved performance [20, p. 82].

With ideas from robotic force control and servomotor control as potential influences, force control was introduced to EMBs. One example is Lidosha Kiki Ptd. Ltd.’s 1986 patent description of an electromechanical disk brake with feedback force control [21].

In more recent work, clamp force control has been implemented on EMBs with embedded control loops for force, motor velocity, and current/torque. Air-gap management in the clearance region has been handled with a transition to outer-loop position control across the contact point between the brake pads and rotor. Recent work on cascaded clamp force control for EMBs is reported in [4]–[11].

B. Cascaded PI Control Architecture

An architecture for cascaded EMB force control is shown in Fig. 5. It has three control loops to regulate the clamp force, motor angular velocity, and the motor current. Each control loop has PI control acting on the tracking error and an integral antiwindup scheme. In this study, conditional integration is imposed on the force and velocity control, while the current control has limited integration. There are protection limits on the set-point commands for the velocity $|\dot{\theta}^*| \leq 300 \text{ rad} \cdot \text{s}^{-1}$ and the motor current $|i_q^*| \leq 40 \text{ A}$. The force, velocity, and current controllers were run at 0.25, 1.25, and 5 kHz, respectively. In practice, the current control may include watchdog protection, back-EMF compensation, and feed-forward decoupling of the quadrature and direct circuits. Some features of the current control were executed at a faster 20 kHz. The power stage of the embedded controller had a (direct current) dc-link converter to operate a three-phase, permanent-magnet synchronous motor. Further details on this class of electrical drive are provided by Leonhard in [20].

C. Tuning the PI Gains

Recent surveys on methods to tune PI differential (PID) controllers may be found in [22] and the references therein. PID control is also widely covered in texts such as [23]. From the various methods for gain selection, an optimal tuning approach was chosen for the present work.

Since the clamp force tracking performance is a function of the controller gains (P_f , I_f , P_v , and I_v), an optimal tuning can be found for a given maneuver by minimizing an appropriate quadratic cost function. The EMB model in Section II was used for optimization. The MATLAB solver “lsqnonlin()” was used with an appropriate search space and initial guess to solve the following nonlinear optimization problem:

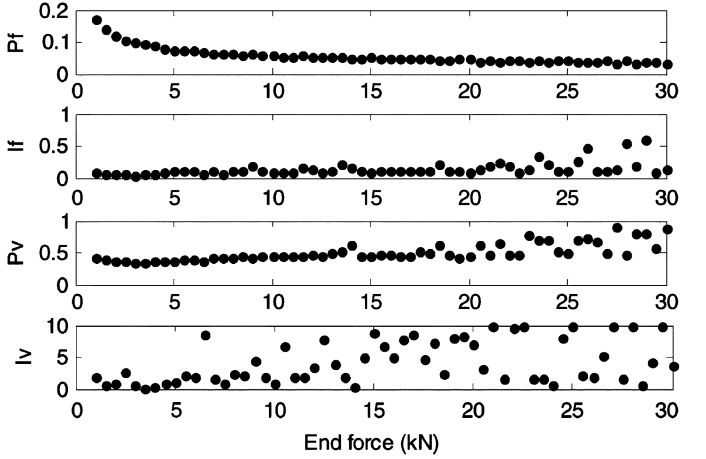


Fig. 6. Optimal PI gains (P_f , I_f , P_v , and I_v) to the various “end forces” from a nominal 0.1-kN start force.

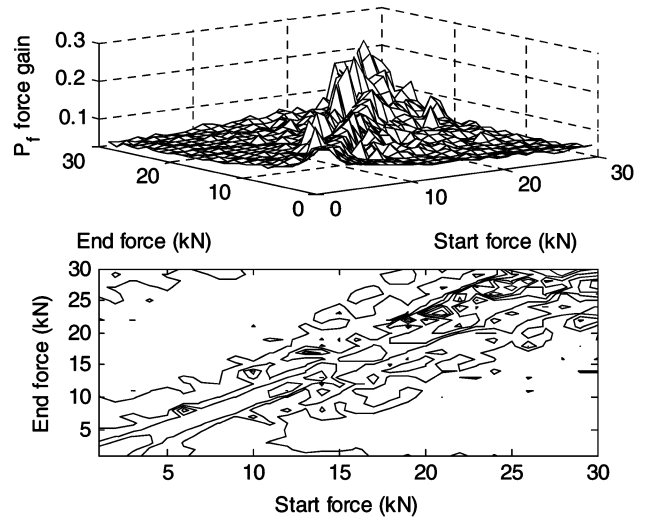


Fig. 7. Surface and contour plot of the optimal proportional force gain P_f for steps defined by the various “start” and “end” forces.

$$\min_{P_f, I_f, P_v, I_v} \sum_{k=1}^n e_{fk} Q e_{fk} + u_{pk}^* R u_{pk}^* \quad (4)$$

where $e_{fk}(P_f, I_f, P_v, I_v) = F_{cl}^* - F_{cl}(P_f, I_f, P_v, I_v)$ is the clamp force tracking error, $u_{pk}^*(P_f, I_f, P_v, I_v) = i_q^* K_t \omega_m^*$ is the power demand, and n is the number of sample instants to the end of the maneuver. The weightings Q and R were selected such that cost on the tracking error was dominant.

Using this optimization approach, the force and velocity PI gains were tuned for an array of step maneuvers throughout the work envelope. Appropriate current control gains were held fixed throughout the maneuvers, with the fast electronic transients having little influence on the slower mechanical dynamics. The set of optimal gains plotted in Fig. 6 correspond to step force applies from a nominal 0.1 kN. The optimal proportional force gain is also plotted in Fig. 7 for the steps defined by the various “start” and “end” force levels. In each case, the initial position was determined from the start force via

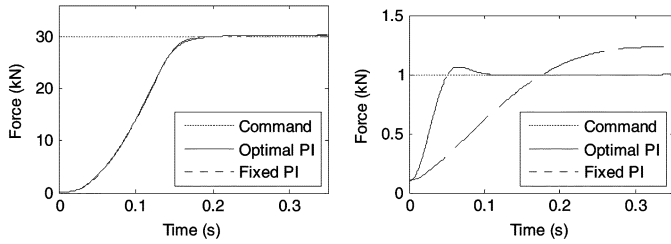


Fig. 8. Large and small magnitude brake apply with fixed gains that are appropriate for the large maneuver.

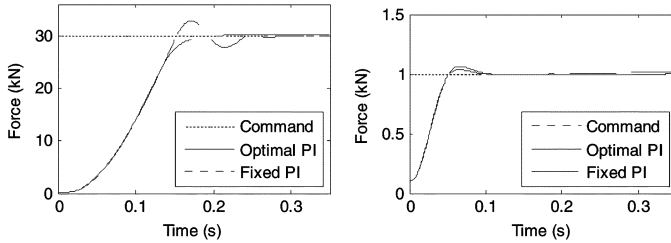


Fig. 9. Large and small magnitude brake apply with fixed gains that are appropriate for the small maneuver.

the stiffness curve. The initial velocity was set finitely small at 0^\pm and with the right heading to avoid the zero velocity state.

Of the four gains, an appropriately tuned proportional force gain P_f was most influential in reducing the optimization cost, followed by the proportional velocity gain P_v and the two integral gains I_f and I_v . The dominant influence of P_f will become apparent in Figs. 8 and 9, where it is adjusted alone to significantly alter the performance. The spread of the numerically optimized gains will increase as their influence on the cost decreases. Thus, due to its dominance, the trend for P_f in Fig. 6 is well established while there is variability in the other gains, particularly I_v .

It should also be noted that the search algorithm has the potential to become stuck in local minima. For example, if the initial guess for the optimal gains is near zero, then the optimization can identify a local solution where the gains are set to zero to minimize the term $u_{pk}^* R u_{pk}^*$. The performance time histories were checked to avoid generating clearly erroneous solutions that may be associated with local minima. The most significant result from the optimal tuning was the trend for the dominant proportional force gain P_f .

In Figs. 6 and 7, it may be observed that the optimal proportional force gain is elevated for small magnitude maneuvers. This is also shown by the high gain ridge in the contour plot. The proportional gain “ridge” is also elevated at higher clamp forces where the system is driven under load. The variation in optimal gain is due to the combined effect of the current saturation, the cost penalty on the power demand, and the increasing significance of friction for fine maneuvers. The proportional force gain also acts to schedule actuator deceleration based on the tracking error. Since the motor torque is limited and greater momentum is developed during large maneuvers, it is then necessary to extend the deceleration period using a smaller proportional force gain. Hence, it is clear that no one set of fixed gains can be close to optimal for all possible steps.

The degree to which suboptimal gain selection can affect closed-loop performance was investigated in simulation. For the example in Fig. 8, a set of fixed gains that is near optimal for a full application ($P_f = 0.034, I_f = 0.15, P_v = 0.51, I_v = 4.2$) is observed to be overly conservative for a light apply.

Conversely, Fig. 9 shows that a set of gains appropriate for a light application ($P_f = 0.17, I_f = 0.15, P_v = 0.51, I_v = 4.2$) result in significant overshoot and increased settling time when used for a larger application.

The cascaded PI control structure in Fig. 5 has been used for EMBs in prior work and on some prototype vehicles. However, with fixed gains, the control cannot cover the operational envelope without substantial degradation in performance relative to the optimal set. Furthermore, the proportional gain ridge in Fig. 7 shows that the optimal gain set varies with the details of the brake maneuver, precluding a simple gain schedule based on the clamp force.

IV. MODIFIED CONTROL ARCHITECTURE

It is apparent that there is substantial opportunity to improve upon the performance of a fixed-gain cascaded PI control for an electromechanical brake. The degraded control performance shown in Section III results from its inability to manage actuator nonlinearity. Load-dependent friction also poses a challenge for fine amplitude maneuvers. Possible improvements may include the addition of derivative control, feed-forward action, or techniques of gain scheduling and feedback linearization.

An extension from P to PID force control was suggested in [10] and [11] to “provide more design freedom in shaping the force dynamics.” However, in simulation, the extra design freedom was not sufficient to maintain a high level of control performance for all brake operations. Also, the derivative action can amplify high-frequency noise. Interestingly, this may actually be beneficial in some scenarios, as it acts like a dither signal to help mitigate the effect of static friction.

Another powerful mechanism for improving the performance of the baseline cascaded PI control is the addition of feed-forward action. The use of feed-forward control is common, and its benefits are advocated in texts such as [20] and [23]. In Fig. 10, for example, a reference generator is included to synthesize commands for the force, velocity, and current. Saturations are applied as before to the commands $\dot{\theta}^*$ and i_q^* for protection. The reference generator may be configured in a number of ways, and a simple example is shown in Fig. 11. It has a feed-forward current command for the computed load, $i_{clref} = F_{cl}^* N / K_t$. Then, to obtain a velocity reference, a filter was first applied to the force command to generate a desirable profile. The filter acts as a profile generator and may be chosen as a second-order transfer function. This generates an achievable or desired response for the second-order actuator. The profiled force was converted to a position by an inverse stiffness function. This was differentiated and adjusted by the gear ratio to give the motor velocity reference $\dot{\theta}_{ref}$.

In simulation, the feedforward reference generator greatly improved the range of over which satisfactory control performance was maintained. However, it was not trivial to create a reference generator that was appropriate for all maneuvers

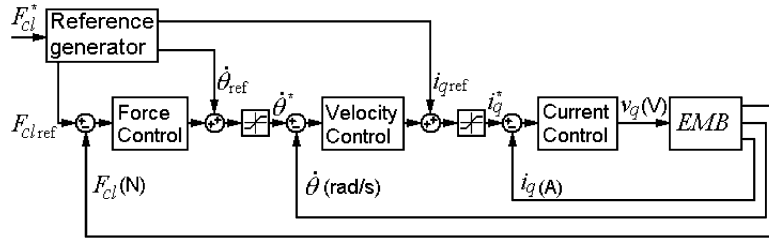
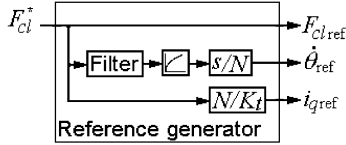


Fig. 10. Cascaded control with reference generator for feed-forward control action.

Fig. 11. Example reference generator to synthesize the reference force F_{cl}^{ref} , velocity $\dot{\theta}_{ref}$, and current command i_{qref} .

throughout the work envelope. For example, the described profile generator tended to overexcite the system and cause overshoot for some small maneuvers. Of course, the simple reference generator may well be improved over a second-order transfer function. A more sophisticated version might include rate limits, an improved system model, scheduling, or some system inverse. Before pursuing a more complex solution, however, the benefits of other control strategies might first be considered. Indeed, it may be possible to address the challenges of actuator nonlinearity more directly by techniques of gain scheduling and feedback linearization.

The method of feedback linearization may be used to directly compensate the nonlinear loads that arise due to friction and the characteristic stiffness. For example, compensation of the static and Coulomb friction torque $T_{s/c}$ may be implemented based on the following model:

$$T_{s/c} = \begin{cases} (C + GF_{cl})\text{sign}(\dot{\theta}), & \forall |\dot{\theta}| > \varepsilon_1 \\ (T_s + GF_{cl})\text{sign}(\dot{\theta}^*), & \text{if } |\dot{\theta}| < \varepsilon_1 \text{ and } |\dot{\theta}^*| > \varepsilon_2 \\ 0, & \text{otherwise.} \end{cases} \quad (5)$$

Here, the small interval defined by $\pm\varepsilon_1$ is used to implement the Karnopp remedy for zero velocity detection [14]. Similarly, a small deadband $\pm\varepsilon_2$ may be defined to avoid unnecessary switching due to noise or otherwise. For generality, if $\dot{\theta}^*$ is not calculated in the control, then the term $\dot{\theta}^*$ may be replaced with $(F_{cl}^* - F_{cl})$ to give the desired heading, or sign, at zero velocity.

A friction-compensating current is determined from the friction model as $i_{qc1}^* = T_{s/c}/K_t$. As discussed, the friction parameters D , C , and G were determined using measurements of the motor torque, velocity, and clamp force. Since the embedded controller has access to these measurements, it may be possible to identify and update the friction parameters online.

Experimental tests were run using the prototype EMB and the fixed-gain PI control, with and without friction compensation. The trials were run back-to-back with the friction compensation either enabled or disabled. Fig. 12 shows the results when the command was a fine 2% modulation about a 25-kN load at a frequency of 4 Hz. It may be observed that there is a significant

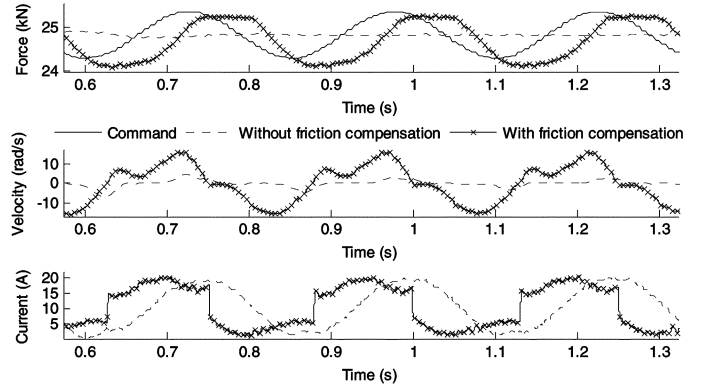


Fig. 12. Measured fixed-gain PI responses with and without friction compensation for a fine 2% modulation about a 25-kN clamp load at 4 Hz.

improvement when the friction compensation is active. While the compensation is not perfect, it is effective in overcoming the lockup due to static friction. In the motor velocity subplot, the catching around zero velocity is mainly avoided when the friction compensation is enabled. Step changes may be observed in the subplot for the motor quadrature current as the friction compensation switches the compensating torque $T_{s/c}$ across the zero velocity threshold.

As a further elaboration, a second compensation term was included in the current command to counteract the load torque disturbance on the motor: it was given by $i_{qc2}^* = F_{cl}N/K_t$. Some comparison may be drawn with the previous feed-forward term for i_{qref} that was based on the command F_{cl}^* rather than the measurement F_{cl} .

While the nonlinear stiffness and the resultant load torque disturbance may be feedback linearized in other manners, the proposed compensation is perhaps the most simple. The total compensating current command is then the sum of the two compensating terms $i_{qc}^* = i_{qc1}^* + i_{qc2}^*$. Since the feedback linearization cannot be perfect, the feedback control K_c offers a mechanism to manage the remaining disturbance.

In addition to the feedback linearization, a precompensating inverse gain was incorporated (a form of gain scheduling [24]) to isolate the controller from the stiffness nonlinearity.

The resultant modified control architecture is shown in Fig. 13. At the plant input, the current command i_q^* was limited to 40 A and then commutated by the power electronics based on measurements of the motor position θ to produce the current i_q . The implementation of the current control was standard and similar to that in [20, p. 334]. The inverse gain was chosen such that the composite stiffness gain was a constant (from

and

$$\mathbf{e}_f = \begin{bmatrix} e_f(k) \\ \vdots \\ e_f(k + H_p) \end{bmatrix}.$$

Here, ρ weights the slack variable, ε , to penalize violation of the soft velocity constraint. The clamp force tracking error at the sample instant k is $e_f(k) = v^*(k) - v(k)$, and the change in the current control is $\Delta i_q^*(k) = i_q^*(k) - i_q^*(k-1)$. The cost function has a penalty on changes in control to avoid chatter. i_{qc}^* and $i_{q\max}^*$ define the hard constraint on the motor current command i_q^* . Ideally, the optimization would consider a dynamic saturation to explicitly allocate the motor current i_{qc}^* , for the parallel operation of the friction compensation and feedback linearization. However, a fixed bound can provide a reasonable approximation for most operation.

The matrices Q and R weight the tracking error and the changes in control input. Their values were selected such that the cost on tracking error was dominant. H_p is the prediction horizon and H_u is the control horizon. A reduced number of control moves H_u may be chosen to decrease the computational demand on an iterative solution. Meanwhile, the prediction horizon H_p may be extended to improve trajectory planning and control stability. For control simulation, the prediction horizon was set to $H_p = 40$. With a control period of 0.004 s, this gave a prediction horizon of 0.16 s and was sufficient to anticipate a full brake apply. The number of control moves was set to $H_u = 20$.

The apparent plant seen by the controller K_c in the modified architecture of Fig. 13 was approximated by the predictive state-space model

$$\begin{aligned} \dot{x} &= \begin{pmatrix} -D/J & 0 \\ NK & 0 \end{pmatrix} x + \begin{pmatrix} K_t/J \\ 0 \end{pmatrix} i_q^* \\ v &= (0 \quad 1)x \end{aligned} \quad (7)$$

where $x = [\dot{\theta}]_v$, v was the linearized force output shown in Fig. 13, and $K = 25.6$ kN/mm was the compound gain of the stiffness and the inverse function. For implementation, (7) was converted to an equivalent discrete time model.

The mechanism of feedback is used to handle imperfection in the predictive model. At each time-step, the initial conditions of the MPC optimization are set using feedback measurements of the state variables $\dot{\theta}$ and v .

Solution of the constrained optimization problem (6) was determined in simulation using MATLAB's model predictive control toolbox with Dantzig–Wolfe's active set method.

Ideally, future knowledge of the desired brake trajectory could be used to improve the tracking performance. However, anticipating the brake demand so that the controller can look ahead may be difficult when the driver's intent is unknown. There may be some potential scenarios where this is possible. For example, it has been suggested that emergency brake maneuvers can be anticipated by a high pedal apply rate during panic braking. Also, some advantage may be possible with antilock brake systems that command brake trajectories rather than a setpoint. Alternatively, a future collision-avoidance program may schedule a brake force trajectory to coordinate an evasive maneuver. While such anticipation is beyond current

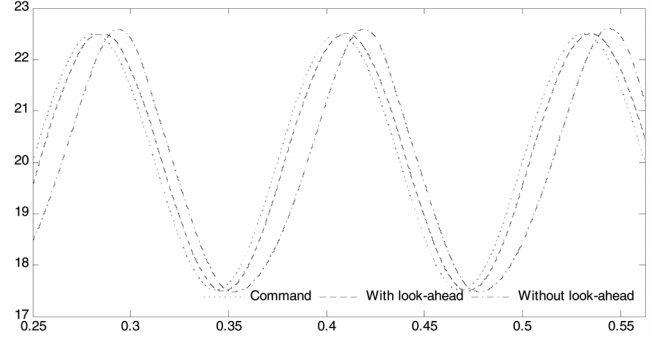


Fig. 14. 5-kN modulation about a 20-kN load at 8 Hz for the constrained MPC with and without look-ahead anticipation of the desired force trajectory.

applications, look-ahead action is investigated to determine the potential for improvement. The simulated results in Fig. 14 indicate that a significant improvement is possible when the planned brake force trajectory is available for look-ahead anticipation. Without anticipation, the performance was degraded as the current brake force demand $v^*(k)$ was simply projected to the prediction horizon, i.e.,

$$v^*(i) = v^*(k), \quad \text{for } i = k, \dots, k + H_p. \quad (8)$$

Other projections such as a first-order hold are possible in place of (8), but the alternatives also have their limitations.

B. Unconstrained MPC for Online Implementation

For practical implementation on the embedded controller of a prototype EMB, it was necessary to reduce the computational load of the MPC. The constraints were relaxed so that an analytic closed-form solution was available for the unconstrained optimization problem

$$\min_{\Delta i_q^*} \left(\mathbf{e}_f^T Q \mathbf{e}_f + \Delta \mathbf{i}_q^{*T} R \Delta \mathbf{i}_q^* \right). \quad (9)$$

To limit the motor current and velocity (for overdrive protection or quick reversal), a dynamic bound was subsequently imposed on the current command

$$\max(i_{q\min}^*, i_{q\dot{\theta}\min}^*(\dot{\theta})) \leq i_q^* \leq \min(i_{q\max}^*, i_{q\dot{\theta}\max}^*(\dot{\theta})). \quad (10)$$

Here, the current command i_q^* was confined to the static range $[i_{q\min}^*, i_{q\max}^*]$ and the velocity-dependent range $[i_{q\dot{\theta}\min}^*(\dot{\theta}), i_{q\dot{\theta}\max}^*(\dot{\theta})]$.

Using the measured velocity $\dot{\theta}$, the dynamic range for $i_{q\dot{\theta}}^*(\dot{\theta})$ was calculated to prevent acceleration beyond the velocity limits over n future control periods of duration T . In other words, the measured velocity and the velocity limits $\dot{\theta}_{\max}$ and $\dot{\theta}_{\min}$ were converted to an approximate acceleration bound $\ddot{\theta}_{\max}(\dot{\theta})$ and $\ddot{\theta}_{\min}(\dot{\theta})$. The motor torque was then constrained in the following manner:

$$J\ddot{\theta}_{\min} \leq T_m - T_L - T_F \leq J\ddot{\theta}_{\max}$$

$$\text{i.e., } J\ddot{\theta}_{\min} + T_L + T_F \leq T_m \leq J\ddot{\theta}_{\max} + T_L + T_F. \quad (11)$$

Here, the friction torque T_F may be neglected conservatively since it opposes motion and always acts to decelerate the system

and reduce the velocity. Hence, the following inequality is sufficient:

$$J\ddot{\theta}_{\min} + T_L \leq T_m \leq J\ddot{\theta}_{\max} + T_L$$

or in approximate terms of the velocity limits

$$\begin{aligned} \frac{J(\dot{\theta}_{\min} - \dot{\theta})}{nT} + F_{cl}N &\leq \\ i_{q\dot{\theta}}^* K_t &\leq \frac{J(\dot{\theta}_{\max} - \dot{\theta})}{nT} + F_{cl}N. \end{aligned} \quad (12)$$

Here, T is the sample period of the controller and n may be set as a small number of intervals, say two, over which acceleration is restricted to avoid velocity overshoot.

Hence, the limits in (10) are given by

$$\begin{aligned} i_{q\dot{\theta}_{\min}}^*(\dot{\theta}, F_{cl}) &= \frac{J(\dot{\theta}_{\min} - \dot{\theta})}{K_t n T} + \frac{F_{cl}N}{K_t} \\ i_{q\dot{\theta}_{\max}}^*(\dot{\theta}, F_{cl}) &= \frac{J(\dot{\theta}_{\max} - \dot{\theta})}{K_t n T} + \frac{F_{cl}N}{K_t}. \end{aligned} \quad (13)$$

The measurements of the clamp force F_{cl} and motor velocity $\dot{\theta}$ are available online.

To maintain consistency between the constraints, the dynamic current limits are restricted by

$$i_{q\dot{\theta}_{\min}}^*(\dot{\theta}) < i_{q\dot{\theta}_{\max}}^*(\dot{\theta}) \text{ and } i_{q\dot{\theta}_{\max}}^*(\dot{\theta}) > i_{q\dot{\theta}_{\min}}^*(\dot{\theta}). \quad (14)$$

The unconstrained optimization problem (9) has a known analytic solution, and its derivation may be found in texts such as [26, pp. 74-81]. The result is that the optimal input changes are given by

$$\Delta \mathbf{i}_q^* = -(\Gamma^T Q \Gamma + R)^{-1} \Gamma^T Q (\Psi - v^*) \quad (15)$$

where the matrices Γ and Ψ are determined by a state-space model and the prediction horizons.

The prediction model of (7) was again used. When (7) is written in the discrete form, then

$$\begin{aligned} x_{k+1} &= Ax_k + Bu_k \\ y_k &= Cx_k \end{aligned} \quad (16)$$

and the quadratic cost function (9) is denoted as

$$J = (v - v^*)^T Q (v - v^*) + \Delta \mathbf{i}_q^{*T} R \Delta \mathbf{i}_q^* \quad (17)$$

with the projected output v , target trajectory v^* , input changes $\Delta \mathbf{i}_q^*$, and penalty weights Q and R given by

$$\begin{aligned} v &= \begin{bmatrix} v_{k+1} \\ \vdots \\ v_{k+H_p} \end{bmatrix} = \begin{bmatrix} C & & 0 \\ & \ddots & \\ 0 & & C \end{bmatrix} \begin{bmatrix} x_{k+1} \\ \vdots \\ x_{k+H_p} \end{bmatrix} \\ &= \Omega \begin{bmatrix} x_{k+1} \\ \vdots \\ x_{k+H_p} \end{bmatrix} \\ v^* &= \begin{bmatrix} v_{k+1}^* \\ \vdots \\ v_{k+H_p}^* \end{bmatrix} \end{aligned}$$

$$\begin{aligned} \Delta \mathbf{i}_q^* &= \begin{bmatrix} \Delta i_{qk}^* \\ \vdots \\ \Delta i_{qk+H_u-1}^* \end{bmatrix} \\ Q &= \begin{bmatrix} Q_1 & 0 & 0 \\ 0 & \ddots & 0 \\ 0 & 0 & Q_{H_p} \end{bmatrix} \\ R &= \begin{bmatrix} R_0 & 0 & 0 \\ 0 & \ddots & 0 \\ 0 & 0 & R_{H_u-1} \end{bmatrix} \end{aligned} \quad (18)$$

then the matrices Γ and Ψ are

$$\begin{aligned} \Psi &= \Omega \begin{bmatrix} A \\ \vdots \\ A^{H_p} \end{bmatrix} x_k + \Omega \begin{bmatrix} B \\ \vdots \\ \sum_{i=0}^{H_p-1} A^i B \end{bmatrix} u_{k-1} \\ \Gamma &= \Omega \begin{bmatrix} B & \cdots & 0 \\ AB + B & \cdots & 0 \\ \vdots & \ddots & \vdots \\ \sum_{i=0}^{H_u-1} A^i B & \cdots & B \\ \sum_{i=0}^{H_u} A^i B & \cdots & A + B \\ \vdots & \vdots & \vdots \\ \sum_{i=0}^{H_p-1} A^i B & \cdots & \sum_{i=0}^{H_p-H_u} A^i B \end{bmatrix}. \end{aligned} \quad (19)$$

In experimentation, the prediction horizon of the unconstrained MPC was set to $H_p = 38$, and the number of control moves was $H_u = 3$. With the discrete control period at 0.004 s, this gave a prediction horizon of 0.152 s and was sufficient to project a full brake apply.

Solving the unconstrained optimization (9) with a post constraint on the input (10) is different to, and less desirable than, solving the constrained optimization problem (6). However, this simplification was necessary for practical implementation given the computational limits of the embedded controller. One limitation of the unconstrained MPC is that, when the control trajectory is recomputed at each time-step, the forecast action may be liable to exceed the actuator limits. The problem can manifest during deceleration and overshoot may occur if the unconstrained MPC overanticipates its access to decelerating torque. To help avoid this scenario, the weight R was increased to impose a greater penalty on the change in input. Consequently, the unconstrained MPC drives the actuator more conservatively than the constrained MPC, as shown in the simulation results of Fig. 15. This behavior is also apparent in the experimental results of Figs. 16 and 17, where the unconstrained MPC executes a conservative deceleration that mostly avoids the current saturation.

To test its performance, the unconstrained MPC with post-constraint was implemented on the embedded controller of the prototype EMB. Trials were run, and the experimental results are presented in Figs. 16-18. For the large brake apply in Fig. 16, there is little improvement with the unconstrained MPC control because the response is mainly limited by actuator constraints. The current is limited up to $t = 0.04$ s, whereas

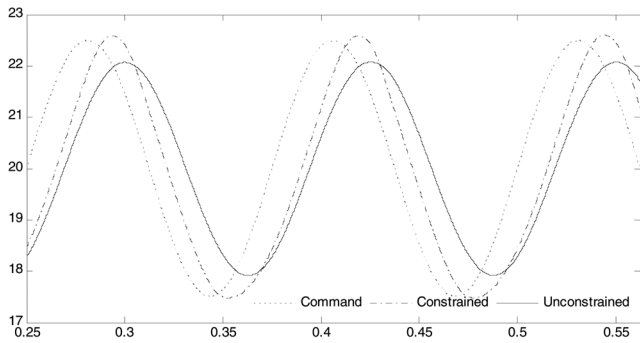


Fig. 15. 5-kN modulation about a 20-kN load at 8 Hz for the constrained and unconstrained MPC. The latter is subject to a more conservative penalty on Δu to help avoid excessive torque demand.

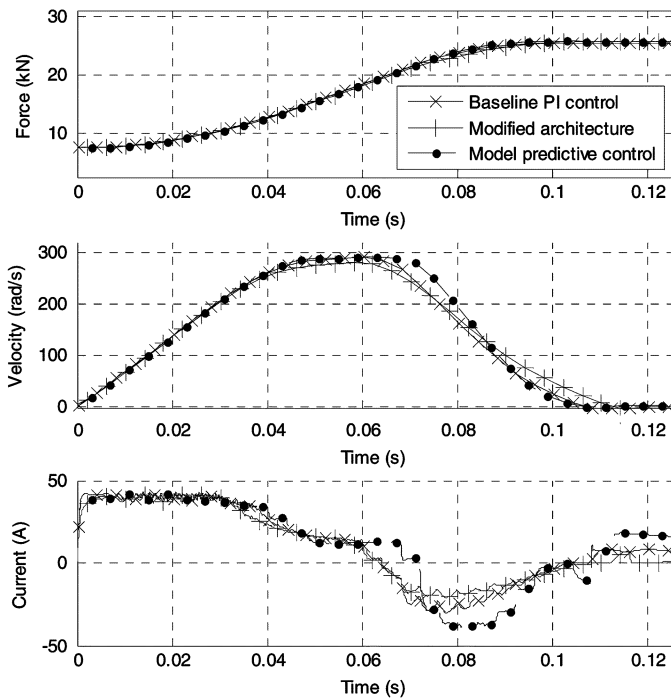


Fig. 16. Large magnitude brake maneuver comparing the measured responses with the fixed-gain PI control, the modified control architecture, and the unconstrained MPC.

after the velocity is limited to approximately $t = 0.06$ s. Only a slight improvement is managed with the unconstrained MPC control by maintaining the maximum velocity for longer and decelerating harder. A more significant improvement is observed for the small magnitude maneuver shown in Fig. 17. Here, a significantly reduced rise time is achieved with the unconstrained MPC (0.019 s) when compared with the modified control (0.035 s), and the baseline cascaded PI control (0.066 s). The improvement is achieved through a better utilization of the available motor torque.

Fig. 18 presents experimental results for a fine 2% modulation about 25 kN at 8 Hz. In this case, the baseline cascaded PI control almost suffers complete frictional lockup due to poor handling of the static friction. The modified control architecture of Fig. 13 offers a significantly improved response due to the management of actuator nonlinearity with inverse gain scheduling and friction compensation. The action of the friction compensation is particularly apparent in the current subplot as the

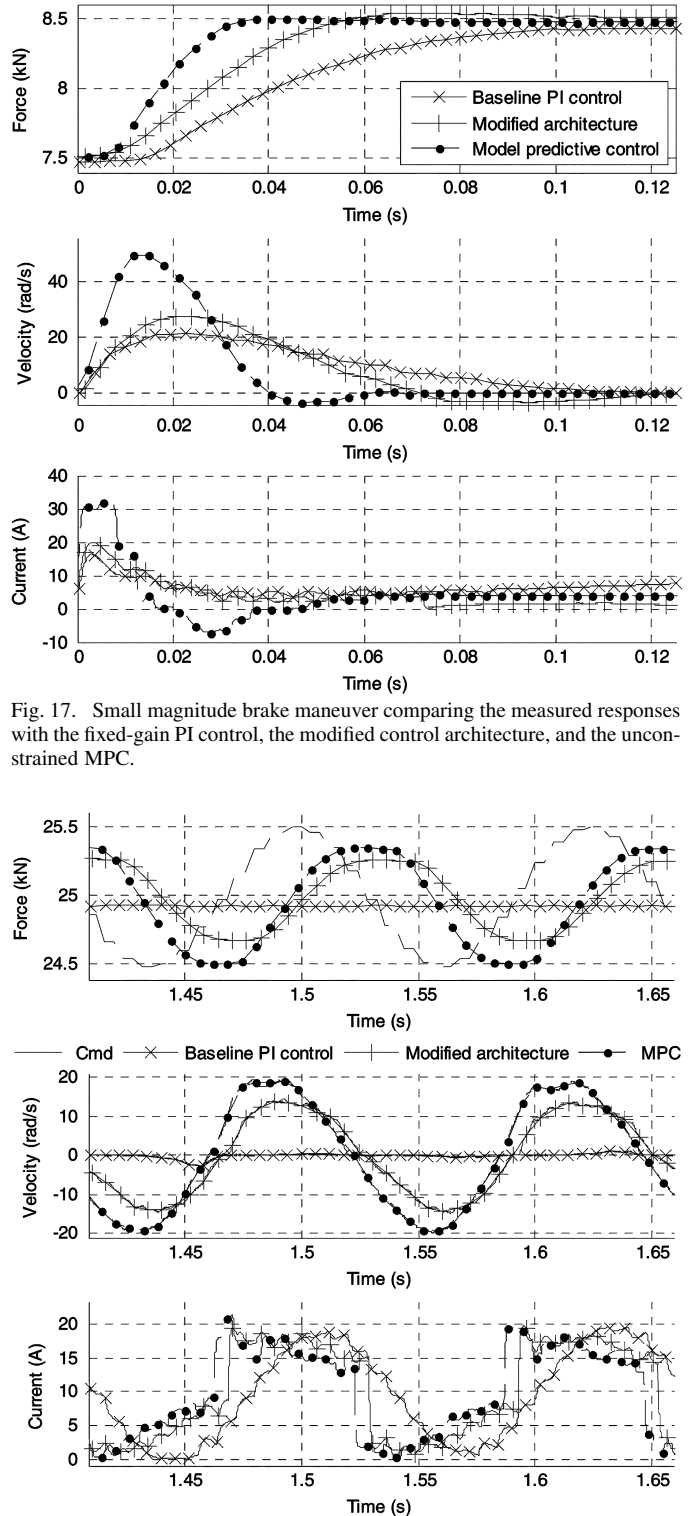


Fig. 17. Small magnitude brake maneuver comparing the measured responses with the fixed-gain PI control, the modified control architecture, and the unconstrained MPC.

Fig. 18. A 2% sinusoidal modulation about 25 kN at 8 Hz comparing the measured performance of the fixed-gain PI control, the modified control architecture, and that with MPC.

compensating torque is switched at each velocity reversal. A further incremental improvement is then achieved when the unconstrained MPC is incorporated within the modified architecture. In comparison to the 2% amplitude that was commanded, the range executed by the unconstrained MPC was approximately 1.7%. This was up from the 1.2% range achieved with the modified control and near 0% with the baseline cascaded PI control.

Lead is also obtained with the unconstrained MPC due to its ability to look ahead. For this modulation, the phase lag was approximately 84° with the unconstrained MPC and 105° with the modified control.

VI. CONCLUSION

In prior work and on some prototype vehicles, a fixed-gain, cascaded PI control has been used to regulate the clamp force of an EMB. However, as a result of the actuator nonlinearity, this control was found to suffer compromised performance across much of the operational envelope. Consequently, a modified control architecture was proposed to manage the actuator nonlinearity with techniques of inverse gain scheduling, friction compensation and feedback linearization. The modified control was tested on a prototype actuator and found to be particularly beneficial for improved fine control. The modified control also provided a structure for the implementation of a MPC. This was found to offer a further improvement in performance by its capacity to look ahead and better utilize the available motor torque. The constrained MPC was demonstrated in simulation. Then, for a practical implementation, the computational demand on the embedded controller of the EMB was reduced by relaxation to an unconstrained MPC with dynamic constraints post-applied.

ACKNOWLEDGMENT

The authors would like to thank and acknowledge the industry partner, Pacifica Group Technologies Pty. Ltd., for the company's continued support. They would also like to thank and acknowledge their sister company PBR Australia Pty. Ltd.

REFERENCES

- [1] N. Wang, A. Kaganov, S. Code, and A. Knudtzen, "Actuating mechanism and brake assembly," PBR Australia Pty. Ltd., World International Property Organization International Publication WO 2005/124180 A1, Dec. 2005.
- [2] H. Hartmann, M. Schautt, and A. Pascucci, "eBrake[®]—The mechatronic wedge brake," *SAE Tech. Paper*, 2002, 2002-01-2582.
- [3] S. Underwood, A. Khalil, and I. Husain, "Switched reluctance motor based electromechanical brake-by-wire system," *Int. J. Vehicle Auton. Syst.*, vol. 2, no. 3/4, pp. 278–296, 2004.
- [4] C. Maron, T. Dieckmann, S. Hauck, and H. Prinzler, "Electromechanical brake system: Actuator control development system," *SAE Tech. Paper*, p. 970814, 1997.
- [5] R. Schwarz, R. Isermann, J. Bohm, J. Nell, and P. Rieth, "Modeling and control of an electromechanical disk brake," *SAE Tech. Paper*, p. 980600, 1998.
- [6] R. Schwarz, R. Isermann, J. Bohm, J. Nell, and P. Rieth, "Clamping force estimation for a brake-by-wire actuator," *SAE Tech. Paper*, 1999, 1999-01-0482.
- [7] R. Schwarz, "Rekonstruktion der Bremskraft bei Fahrzeugen mit elektromechanisch betätigten Radbremsen," Ph.D. dissertation, Institut für Automatisierungstechnik, Technischen Universität Darmstadt, Darmstadt, Germany, 1999.
- [8] R. Isermann, "Electromechanical Disc Brake (EMB)," in *Mechatronic Systems Fundamentals*. London, U.K.: Springer-Verlag, 2003, pp. 560–568.
- [9] C. Line, C. Manzie, and M. Good, "Control of an electromechanical brake for automotive brake-by-wire systems with an adapted motion control architecture," *SAE Tech. Paper*, 2004, 2004-01-2050.
- [10] P. Krishnamurthy, W. Lu, F. Khorrami, and A. Keyhani, "A robust force controller for an SRM based electromechanical brake system," presented at the Proc. 44th IEEE Conf. Decision Control/Eur. Control Conf., Seville, Spain, 2005.
- [11] W. Lu, "Modeling and control of switched reluctance machines for electromechanical brake systems," Ph.D. dissertation, Electr. Comput. Eng., Ohio State Univ., Columbus, 2005.
- [12] R. Roberts, M. Schautt, H. Hartmann, and B. Gombert, "Modelling and validation of the mechatronic wedge brake," *SAE Tech. Paper*, 2003, 2003-01-3331.
- [13] J. Kwak, B. Yao, and A. Bajaj, "Analytical model development and model reduction for electromechanical brake system," presented at the 2004 ASME Int. Mech. Eng. Congress and Exposition, Anaheim, CA, 2004, unpublished.
- [14] H. Olsson, K. J. Åström, C. C. de Wit, M. Gäfvert, and P. Lischinsky, "Friction models and friction compensation," *Eur. J. Control*, vol. 4, no. 7, pp. 176–195, 1998.
- [15] A. Stevens and W. S. Penney, "Improvements in or Relating to Brakes for Vehicles," Great Britain Patent GB189914975, 1899.
- [16] E. A. Sperry, "Improvements in or Relating to Motor Road Vehicles and Devices for Controlling the Various Operations Relating to Starting, Stopping, Accelerating, and Retarding the Same," United States Patent GB189901116, 1899.
- [17] G. R. Wadsworth, "Electrically-Operated Brake," USA U.S. Patent 1104586, 1914.
- [18] D. E. Whitney, "Historical perspective and state of the art in robot force control," presented at the IEEE Int. Conf. Robot. Autom., 1985, presented at.
- [19] J. D. Schutter, "A study of active compliant motion control methods for rigid manipulators based on a generic scheme," presented at the IEEE Int. Conf. Robot. Autom., Raleigh, NC, 1987, presented at.
- [20] W. Leonhard, *Control of Electrical Drives*, 3rd ed. Berlin, Germany: Springer, 2001.
- [21] R. Ohta and M. Kobayashi, "Brake Apparatus," U.S. Patent No. 4 602 702, Jul. 29, 1986.
- [22] M. H. Moradi, "New techniques for PID controller design," presented at the IEEE Conf. Control Applic., Istanbul, Turkey, 2003, presented at.
- [23] K. J. Åström and T. Häggglund, *Advanced PID Control*. Research Triangle, NC: ISA, 2006.
- [24] W. J. Rugh and J. S. Shamma, "Research on gain scheduling," *Automatica*, pp. 361401–1425, 2000.
- [25] M. Vašak, M. Baotic, M. Morari, I. Petrovic, and N. Peric, "Constrained optimal control of an electronic throttle," *Int. J. Control*, vol. 79, no. 5, pp. 465–478, 2006.
- [26] J. M. Maciejowski, *Predictive Control with Constraints*. London, U.K.: Pearson Education, 2002.



problems.

Chris Line received the B.Eng. degree (with first class honors) from the University of Tasmania, Tasmania, Australia, in 2002, and the Ph.D. degree from Department of Mechanical Engineering, The University of Melbourne, Melbourne, Australia, in 2007. His doctoral work focused on investigating electromechanical brake modeling and control with the Research Centre for Advanced By-Wire Technologies.

His current research interests lie in the applications of advanced control techniques to real-world



Chris Manzie received the B.S. degree in physics and the B.S. degree in electrical and electronic engineering and the Ph.D. degree from The University of Melbourne, Melbourne, Australia, in 1996 and 2001, respectively. His doctoral work focused on investigating intelligent control of air fuel ratio in automotive engines.

Since 2003, he has been with the Department of Mechanical and Manufacturing Engineering, University of Melbourne, where he is currently a Senior Lecturer. He was a Visiting Scholar with the University of California, San Diego, in 2007. His research interests lie in model-based and adaptive control with application to powertrain and vehicle dynamics. In 2006, he helped establish the Advanced Centre for Automotive Research and Testing with Ford Australia and the University of Melbourne and is a member of the Research Centre for Advanced By-Wire Technologies.



Malcolm C. Good received the Ph.D. degree in mechanical engineering from The University of Melbourne, Melbourne, Australia, in 1975.

Previously, he was Program Leader for Integrated Manufacture with the Division of Manufacturing Technology of the Commonwealth Scientific and Industrial Research Organisation (CSIRO), Melbourne, Australia. From 1992 to 1996, he was Head of the Mechanical and Manufacturing Engineering Department, University of Melbourne, where he is currently a Professor of Mechanical and Manufacturing Engineering. He has held visiting appointments at the Institute for Sound and Vibration Research (ISVR) of the University of Southampton, Southampton, U.K., the Highway Safety Research Institute (HSRI) of the

University of Michigan, Ann Arbor, General Electric Corporate Research and Development, Schenectady, NY, and Cambridge University, Cambridge, U.K. His research has been in the fields of fluid mechanics, vehicle and machine dynamics, highway geometrics, human factors of automobile and motorcycle control, vehicular impact with roadside structures, dynamics and control of machine tools and industrial robots, and, most recently, automotive drive-by-wire technologies.

Prof. Good has been President of the Australian Robot Association, Australian Contact Person for the International Advanced Robotics Program, and Interim Director of the Advanced Engineering Centre for Manufacturing, and he is currently a Program Leader and Board Member of the Research Centre for Advanced By-Wire Technologies, University of Melbourne.